Nanoscale

PAPER

View Article Online
View Journal | View Issue

Cite this: *Nanoscale*, 2025, **17**, 6580

$Zn_{0.5}Cd_{0.5}Se$ quantum dot-integrated MOF-derived C/N–CeO_2 photocatalyst for enhanced H_2O_2 production and O_2 evolution reactions†

Jayashree Panda, Jyotirmayee Sahu and Kulamani Parida *

Herein, a rational strategy is presented to reduce the sluggish reaction kinetics and inefficient charge carrier separation of heterojunctions while enhancing their opto-electronic properties. A 1D–0D heterojunction, *i.e.*, MOF-derived C/N–CeO_2/$Zn_{0.5}Cd_{0.5}Se$ quantum dot (CZCSe-1) hybrid material, was constructed to address the limitations associated with the H_2O_2 production and O_2 evolution reactions through a facile reflux treatment. As anticipated, the optimised CZCSe-1 composite exhibited an impressive H_2O_2 production rate of 2820.43 μmol g^{-1} h^{-1}, which was 1.7- and 2.1-fold higher than those of pristine C/N–CeO_2 and ZCSe, respectively, and it exhibited stability up to four cycles. Additionally, an O_2 evolution rate of 234.89 mmol g^{-1} h^{-1} was recorded for CZCSe-1, which showed superior activity over other materials previously reported in the literature. It was revealed that the outstanding photocatalytic performance was attributed to the effective anchoring of 0D ZCSe onto vacancy-rich C/N–CeO_2 nanorods, displaying improved charge separation as obtained from the PL, EIS, TPC and maximized redox capability analyses. The charge transfer dynamics in the CZCSe-1 composite *via* the S-scheme heterojunction was further investigated through free radical detection (ESR analysis) and work function study (VB-XPS). This work offers a new approach for optimizing economic metal oxide-based photocatalysts for H_2O_2 production and other applications.

Received 20th January 2025,
Accepted 2nd February 2025

DOI: 10.1039/d5nr00287g

rsc.li/nanoscale

1. Introduction

Hydrogen peroxide (H_2O_2) is an essential chemical with wide range of applications in organic synthesis, chemical industry, and environmental remediation.[1] Recently, H_2O_2 has received great attention as a potential substitute for electricity generation and as a novel energy storage mechanism.[2] The huge demand for H_2O_2 has directed attention towards its synthetic route; meanwhile, 95% of H_2O_2 is produced *via* the indirect oxidation of anthraquinone, which is an energy-intensive reaction and emits toxic by-products.[1,3–6] As a greener alternative, photocatalytic production of H_2O_2 using semiconductor catalysts is convincing because it uses water and oxygen as the chemical source and sunlight as the energy input.[7] At present, the photocatalytic H_2O_2 production process is limited by the narrow solar light adsorption range, inefficient charge carrier separation, and sluggish reaction kinetics.[8] At the same time, artificial photosynthesis and photoelectrochemical water splitting benefit significantly from O_2 evolution.[9] Thereby, the ingenious design of photocatalysts with suitable band gaps, high conductivity, and robust kinetics is highly desirable.

Out of the plentiful semiconducting materials, metal oxides are high-performance photocatalysts owing to their inherent properties like stability, natural abundance, non-toxicity, and low cost.[6,10–15] In particular, CeO_2 is less explored in the area of photocatalytic H_2O_2 production because it mostly responds to UV light owing to its wide band gap (3.1–3.3 eV).[9,13] Therefore, adopting suitable methods for CeO_2 synthesis over conventional ones can be more beneficial in terms of narrow band gap, porosity, specific surface area, and stability.[12,16] Furthermore, unique properties like ultra-high specific surface area, exceptional porosity, structural diversity, and chemical and thermal stability have made metal–organic frameworks (MOFs) an ideal template material to derive metal oxides while preserving their structural traits.[12,16,17] Additionally, nonmetals (such as N and S) doped from the MOF precursor in the derived system enhance the visible light absorption capacity by narrowing the band gap compared to the traditionally prepared metal oxides.[17] Nevertheless, the photogenerated e^- and h^+ in individual CeO_2 tend to recombine, which in turn reduces the photocatalytic efficacy.[9] Therefore, achieving effective spatial exciton separation while maintaining the potent redox capability of the photocatalyst is the key to enhancing H_2O_2 production and O_2

Centre for Nano Science and Nanotechnology, Siksha 'O' Anusandhan (Deemed to be University), Bhubaneswar-751030, Odisha, India. E-mail: kulamaniparida@soa.ac.in, kulamaniparida@soauniversity.ac.in, paridakulamani@yahoo.com; Fax: +91-674-2581637, +91-674-2350642; Tel: +91-674-2379425, +91-674-2351777

† Electronic supplementary information (ESI) available. See DOI: https://doi.org/10.1039/d5nr00287g

evolution. In this regard, an S-scheme heterojunction represents a two-in-one approach towards efficient charge segregation and robust redox capabilities.

The S-scheme heterojunction usually consists of photocatalysts for both reduction and oxidation processes, each having a different work function and staggered band structure. Unequal Fermi levels induce the energy band bending followed by the formation of a built-in-electric field, both acting as the driving force for the transport of photogenerated charge carriers.[18] Consequently, the photogenerated e^- and h^+ on the semiconductor, which possess stronger redox abilities, remain available to participate in the respective photoreactions by the accumulation of ineffective excitons. Further, semiconductor quantum dots (QDs) have become a renowned photocatalytic nanomaterial owing to the size-dependent bandgap, quantum confinement effect, high photoluminescence quantum yield, easy surface modification, multiple exciton generation, high surface-to-volume ratio and exceptional stability.[5,18–20] $Zn_{0.5}Cd_{0.5}Se$ (ZCSe), a representative alloyed quantum dot, exhibits a narrow bandgap in the visible region, quantum size effect, photochemical stability, and competing optoelectrical properties.[21] As compared to C/N–CeO_2, ZCSe acts as a more powerful reduction photocatalyst, and its integration with the MOF-derived C/N–CeO_2 is expected to build a desirable S-scheme heterojunction with effective separation of efficient photoexcited charge carriers.[3,22–24]

To achieve the aforementioned objectives, we herein synthesized Ce–MOF *via* a simple solvothermal technique. Subsequently, C/N–CeO_2 was obtained by annealing the as-synthesized Ce–MOFs in a muffle furnace for 2 h at 450 °C under an ambient air atmosphere. Finally, the ZCSe-anchored defect-induced C/N–CeO_2 nanohybrid was fabricated by a facile one-pot method utilizing TGA as a capping agent, represented schematically in Scheme 1. The opposing surface charges of the constituent materials, suitable energy level positions, and superior charge transfer efficiency are considered the three pillars of the fabricated binary hybrid. Notably, under visible light (λ > 420 nm), the CZCSe-1 sample presents the optimal H_2O_2 and O_2 production rates of 2820.43 μmol g^{-1} h^{-1} and 234.89 mmol g^{-1} h^{-1}, respectively, with stability up to the fourth cycle of photocatalytic reactions. The boosted performance demonstrated by the best photocatalyst, CZCSe-1, could be ascribed to the larger active surface area, higher life span of the excitons, presence of oxygen vacancies (OVs), and higher photo response. The reaction pathway was confirmed by an active species trapping experiment and ESR results. Thus, this work offers a novel perspective on the pathway for developing advanced S-scheme-based systems for a wide variety of photocatalytic applications.

2. Results and discussion

2.1. Synthesis and characterization

Typically, CZCSe-*x* could be obtained *via* a reflux treatment, where the ZCSe gets deposited on the C/N–CeO_2, which is obtained from the pyrolysis of Ce–MOF at 450 °C.[5,25] As a result, a dark maroon product well dispersed in water was obtained, which is required for various photocatalytic applications like O_2 reduction reaction and O_2 evolution reaction *via* water splitting. The structural formation was confirmed by X-ray diffraction (XRD) patterns and Raman spectra, as shown in Fig. 1(a) and (b), respectively. Fig. 1(a) displays the dominant CeO_2 diffraction peaks located at 2θ = 28.6°, 33.1°, 47.6°, and 56.4°, corresponding to the (111), (200), (220), and (311) crystal planes, respectively, which were obtained in pristine C/N–CeO_2 and CZCSe-*x* composites.[9,13,25] Furthermore, the distinct peaks for neat ZCSe obtained at around 2θ = 26°, 43.3°, and 51° were well indexed to the (111), (220), and (311) crystal planes, respectively.[26,27] Interestingly, the intensity of peaks at 26°, 43.3°, and 51° increases with the increased amount of ZCSe in composites, which indicates the successful fabrication of the CZCSe-*x* composites. A close inspection of the XRD profile reveals that the peak intensities of CeO_2 in the composites became weaker and slightly shifted to smaller angles as compared to that of the parent materials, signifying uniform distribution of ZCSe QDs on C/N–CeO_2 nanorods.[28] No other prominent peak in the XRD pattern of the composites was found, which suggested the good crystallinity and high purity of the samples.[28] In addition, the XRD spectrum of C/N–CeO_2 was compared with neat CeO_2 (Fig. S1(b and c)†). The observed shifting of the peak position to higher angles was attributed to the lattice strain caused by smaller ionic radii of C and N, which indicates the doping of nonmetals.[29–31] Further, Raman analysis was proposed to assess the microstructural imperfection in the crystal. The characteristic peak at 464 cm^{-1} was particularly ascribed to the F_{2g} band, while the D-band (defect band) of C/N–CeO_2 was verified by the peaks at 273 cm^{-1} and 587.5 cm^{-1}.[9,25] In addition, the broad peak at around 200–240 cm^{-1} in CZCSe-1 could be due to the first longitudinal optical phonon (1LO) mode of CdSe (207 cm^{-1}) and phonon modes of ZnSe (243 cm^{-1}).[21,32,33] Further, the analysis confirmed that the slight deviation in the peak position of CZCSe-1 is due to lattice expansion and defect generation.[9] Fig. 1(c) shows the FTIR spectra of all the synthesized materials. According to the literature, the broad band in the spectra (3350–3500 cm^{-1}) of all synthesized materials appeared mainly due to stretching vibrations of O–H and N–H bonds.[25,34] The band at around 460 cm^{-1} is due to the deformation mode of the Ce–O bond.[35] A peak at around 2350 cm^{-1} reveals the stretching vibration of C–O adsorbed from the atmospheric CO_2, whereas the other peak at approximately 1640 cm^{-1} indicates the stretching vibration of the C═O group of TGA.[35,36] Additionally, Fig. 1(d) displays the electron spin resonance (ESR) spectrum of CZCSe-1, which characterizes the presence of oxygen vacancies. Herein, a specific response close to the *g* value of 2.001 in CZCSe-1 was observed. In CeO_2, Ce is mostly present in its stable oxidation state, *i.e.*, Ce^{4+}. When Ce^{4+} is reduced to Ce^{3+} due to defect formation (oxygen vacancy), the unpaired electron in the 4f orbital of the Ce^{3+} ion contributes to the ESR signal. In addition, oxygen vacancies in CeO_2 create localized unpaired electrons that are trapped in

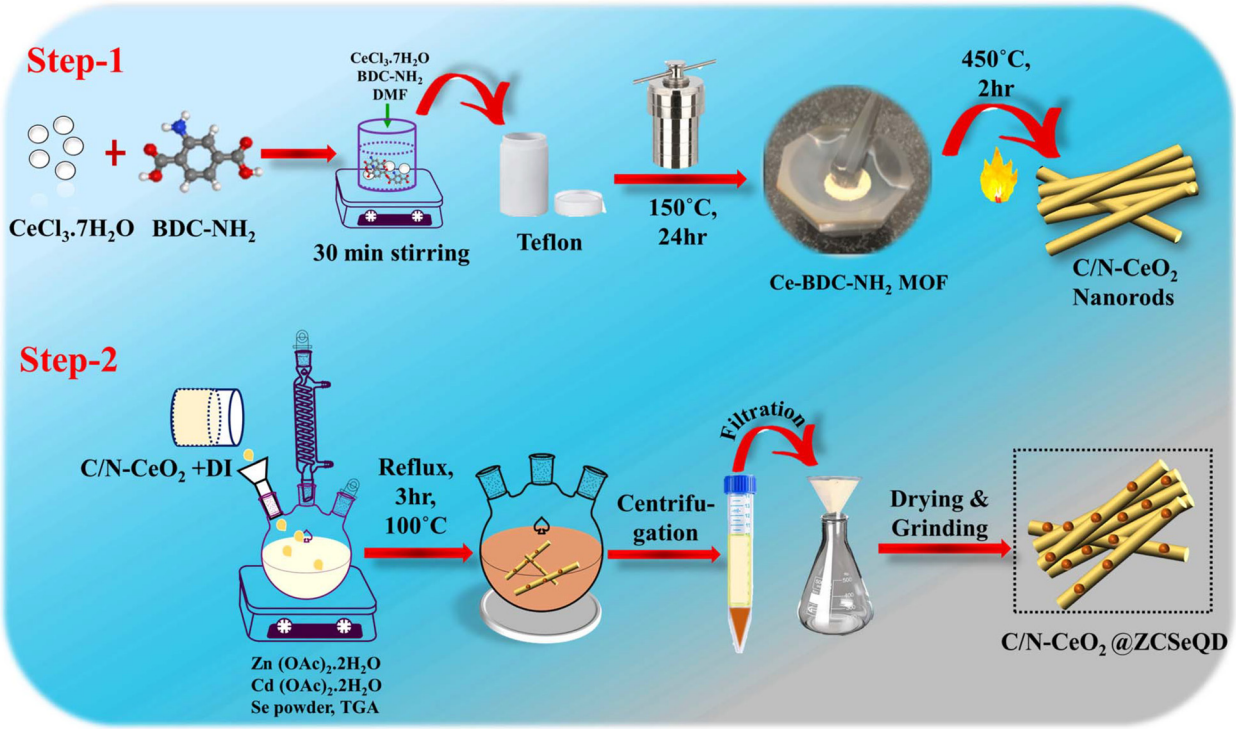

Scheme 1 Schematic of the synthesis method of (Step-1) C/N–CeO_2 and (Step-2) CZCSe composites.

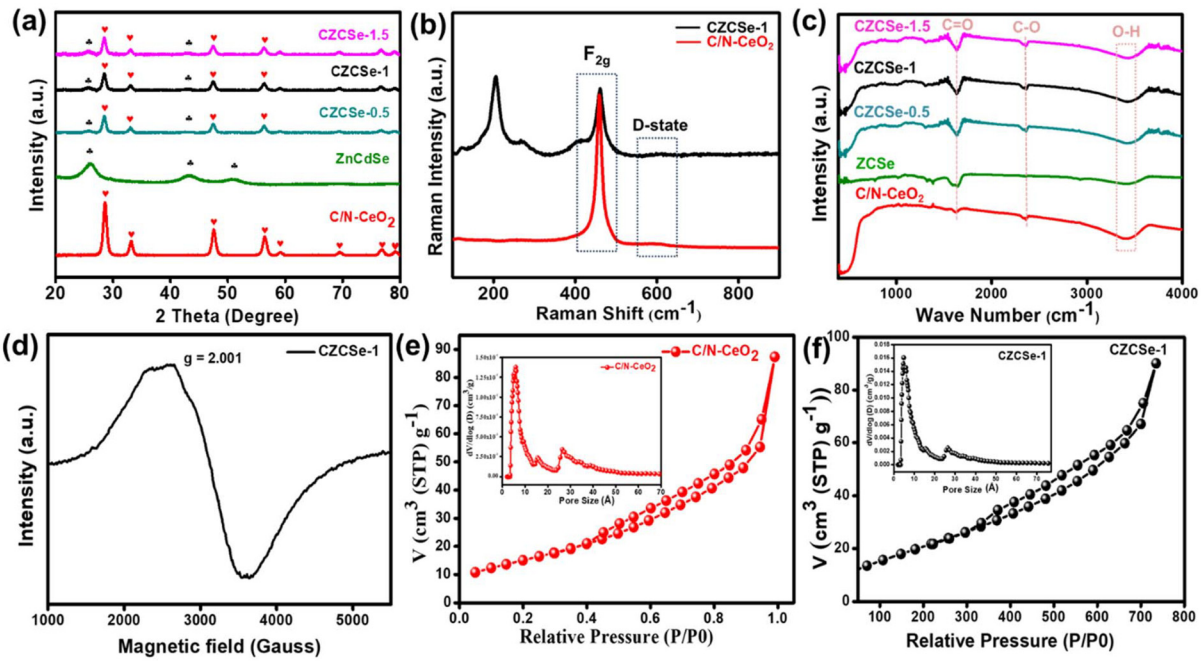

Fig. 1 (a) XRD spectra of C/N–CeO_2, ZCSe, and CZCSe-*x* composites, (b) Raman spectra of C/N–CeO_2 and CZCSe-1, (c) FT-IR spectra of C/N–CeO_2, ZCSe, and CZCSe-*x* composites, (d) EPR spectrum of CZCSe-1, and (e) and (f) BET and BJH plots of C/N–CeO_2 and CZCSe-1.

the vacancy site. Thus, the peak represents the overlapping peak in the ESR spectra.[25,37] Besides, for C/N–CeO_2, a strong symmetrical signal was observed at 340 mT, corresponding to $g \sim 1.97$ (Fig. S2†). This suggested an ideal paramagnetic centre formed by the trapping of an electron near the surface of the redox couple (Ce^{3+}/Ce^{4+}) to form Ce^{4+}–VO–Ce^{3+}.[38]

The porosity and specific surface area were determined by measuring the nitrogen sorption isotherms on fully activated samples at 77 K. The Brunauer–Emmett–Teller (BET) surface area of CZCSe-1 was determined to be 80.2 $m^2\ g^{-1}$, which was notably higher than that of neat C/N–CeO_2 (57.5 $m^2\ g^{-1}$) and ZCSe (59.65 $m^2\ g^{-1}$), as shown in Fig. 1(e and f) and in Fig. S3.† Moreover, CZCSe-1 exhibited a type-IV isotherm (H3 hysteresis loop), with many mesopores (size <50 nm), in agreement with the pore size distribution curve.[9,12,25] The high surface area of the photocatalyst CZCSe-1 estimated the presence of more exposed reaction sites, which probably played a key role in the adsorption and activation of the reduced molecules. However, the neat C/N–CeO_2 and ZCSe displayed a type-IV isotherm showing a micro- and meso-porous architecture.

Typically, the surface elemental composition and oxygen vacancies (OVs) of the photocatalysts are examined by X-ray photoelectron spectroscopy (XPS). The XPS survey spectra in Fig. S4† reveal the presence of C, N, Ce, and O in C/N–CeO_2 and C, N, Ce, O, Zn, Cd, and Se in CZCSe-1. In Fig. 2(a), three distinct peaks at 284.6, 285.9, and 289.0 eV are ascribed to the C=C, C–N, and C–OH bonds of C 1s, while the core level N 1s XPS spectra (Fig. 2(b)) deconvoluted into two peaks at 399.2 eV and 401.1 eV, confirming the substitutional nitrogen in the O–Ce–N structure and the interstitial N state in the sample, respectively.[4,6,9,10,25,37,39] Moreover, two types of deconvoluted peaks are observed in the O 1s spectra (Fig. 2(c)), and the peaks at 529.2 and 531.0 eV are assigned to the C–O and OVs species, respectively.[6,9,25] The OV peak in the CZCSe-1 composite is notably amplified, which is required to supply additional adsorption sites for the photocatalytic activity.[13,25,40] The spin–orbit coupling between the $3d_{5/2}$ (represented as U) and $3d_{3/2}$ (represented as V) term symbols may be responsible for the complex XPS spectra of Ce 3d (Fig. 2(d)). The V′ and U′ peaks are assigned to Ce in the +3 oxidation state, while all other peaks are assigned to Ce in the +4 oxidation state.[16,17] By calculating the area under each peak in the Ce 3d spectrum and using eqn (1), the relative concentration of Ce^{3+} to Ce^{4+} in CZCSe-1 was determined to be nearly 34%, which was around 22% in the case of pristine C/N–CeO_2.[41] This result confirms that CZCSe-1 contains a significant number of OVs, as previously revealed by Raman and EPR studies.

$$\text{Relative conc. of } Ce^{+3}(\%) = A(Ce+3)/[A(Ce+3)+A(Ce+4)] \times 100 \quad (1)$$

Moreover, the peaks at 1044.8 and 1021.7 eV correspond to Zn $2p_{1/2}$ and Zn $2p_{3/2}$ of Zn^{2+} in ZCSe (Fig. 2(e)), and the peaks

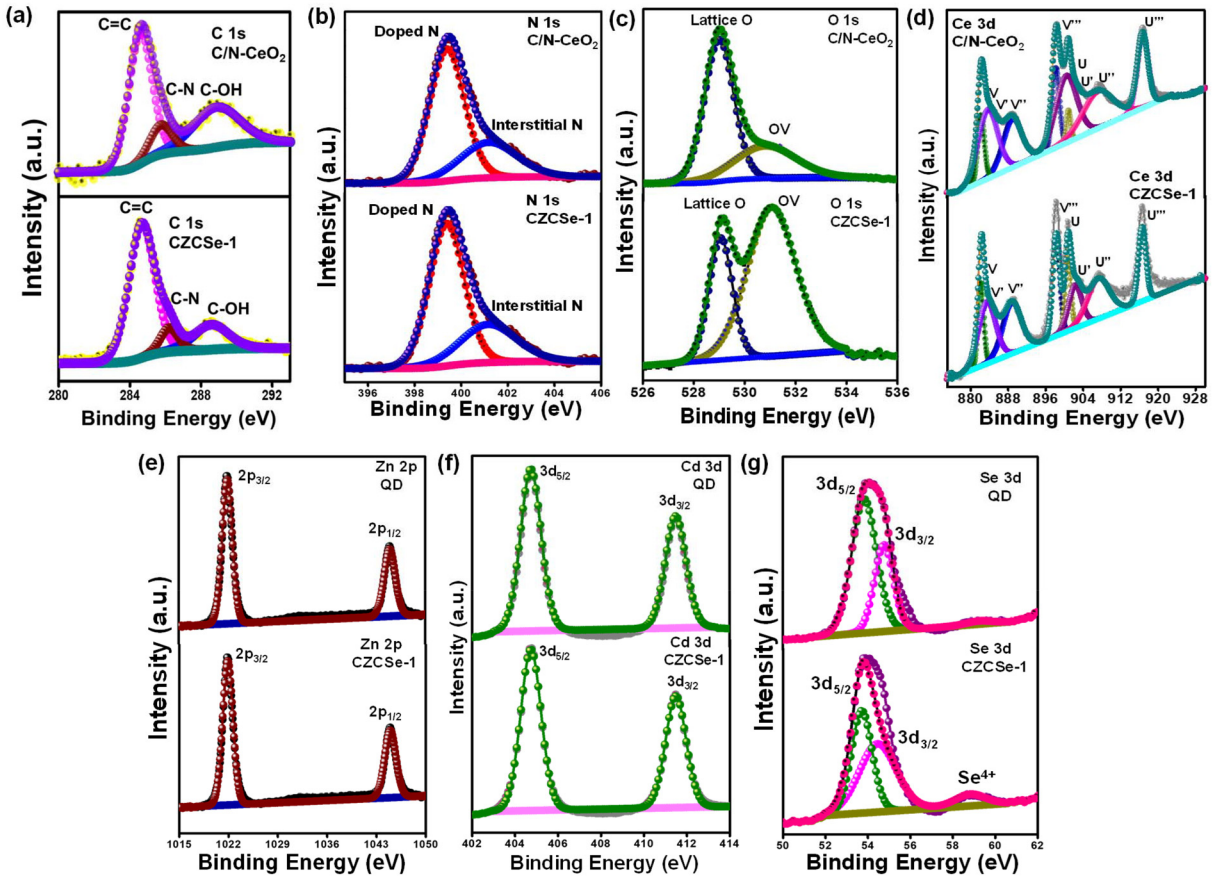

Fig. 2 High resolution XPS spectra of C/N–CeO_2, ZCSe, and CZCSe-1: (a) C 1s, (b) N 1s, (c) O 1s, (d) Ce 3d, (e) Zn 2p, (f) Cd 3d, and (g) Se 3d.

at 411.8 and 405.0 eV can be attributed to Cd $3d_{3/2}$ and Cd $3d_{5/2}$ of Cd^{2+} (Fig. 2(f)).[19,21] In the XPS spectra of Se 3d, the binding energy of the two peaks at 54.5 and 53.7 eV can be attributed to Se $3d_{3/2}$ and Se $3d_{5/2}$ (Fig. 2(g)).[21] Notably, in CZCSe-1, one prominent peak was observed at 59.3 eV in the Se 3d spectra corresponding to Se^{4+}, which offers extra electronic states in the bandgap of materials, thereby narrowing the bandgap and enhancing the photocatalytic activity due to the extended absorption range.

Moreover, the transport of electrons at the interface of the composite material CZCSe-1 can be explored by analyzing the XPS spectra. As observed from the individual spectrum, there is a slight +ve deviation of Ce, O, and C than that of pristine C/N–CeO_2 and a slight −ve deviation of Cd, Zn, and Se that that of neat ZCSe in terms of the binding energy values, which represents a change in the electron density of distinct materials inside the heterostructure due to the transfer of electrons from C/N–CeO_2 to ZCSe. This lowers the binding energy value by increasing the electron density on the ZCSe surface and vice versa.[25,42] These findings corroborate the XRD analysis by confirming the effective interaction of two pure materials and the construction of an n–n heterojunction. Moreover, zeta potential measurements show that ZCSe has a negative surface charge while the pristine C/N–CeO_2 carries a positive surface charge (Fig. S5†), indicating that both display strong electrostatic attraction towards each other, which is valuable for the n–n binary hybrid formation.[25]

Further, to elucidate the role of ZCSe on C/N–CeO_2 nanorods during crystal growth, we monitored the morphology of the hybrid composite using FESEM. In Fig. 3(a), the morphology of pristine C/N–CeO_2 exhibits a rod-like structure. Additionally, the morphology of the hybrid composite CZCSe-1, as shown in Fig. 3(b), illustrates bundles of C/N–CeO_2 nanorods enwrapped with multiple dots, thereby undoubtedly indicating the formation of the CZCSe-1 heterostructure, as further confirmed by transmission electron microscopy (TEM) analysis

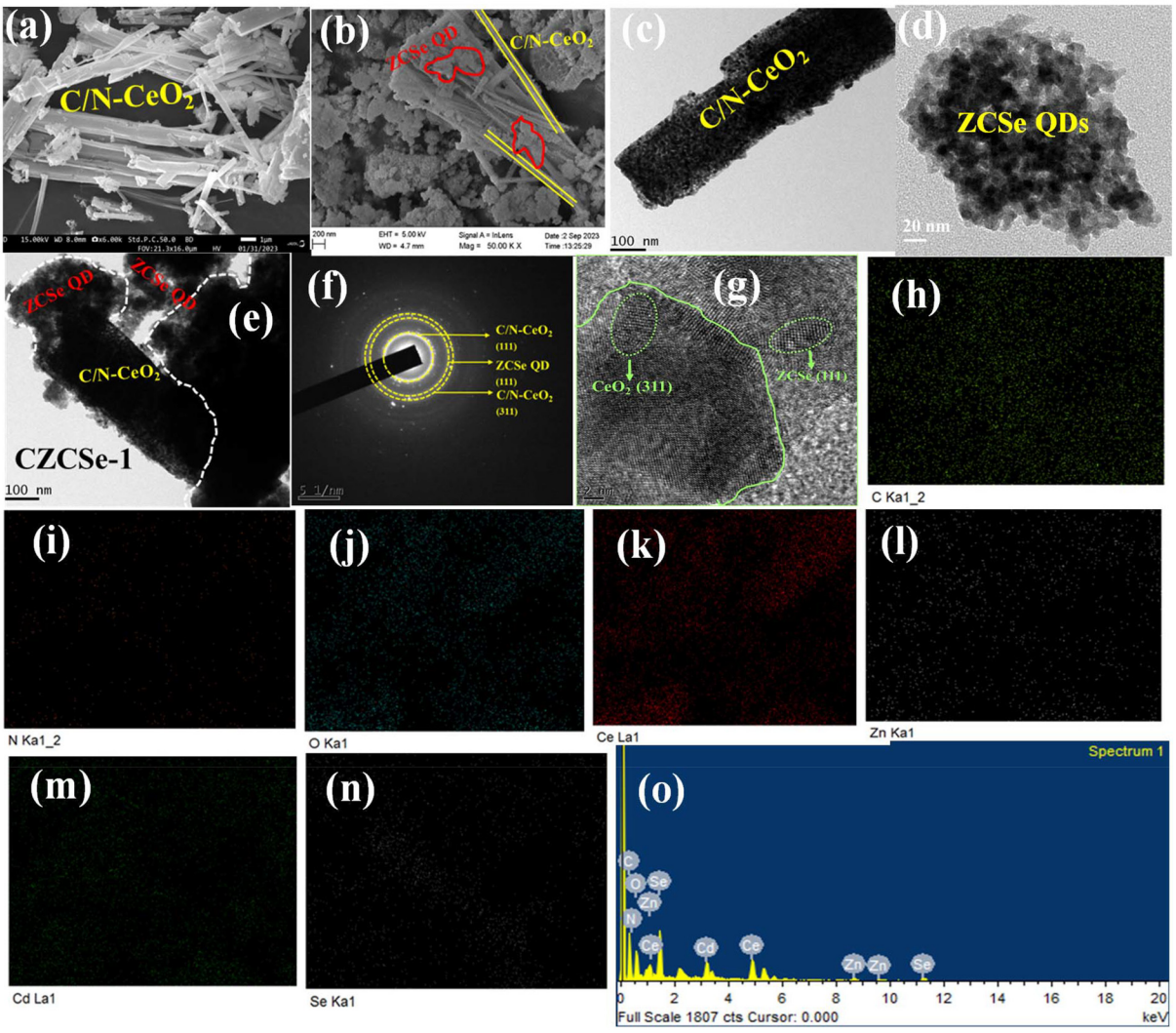

Fig. 3 FESEM images of (a) C/N–CeO_2 and (b) CZCSe-1, TEM images of (c) C/N–CeO_2, (d) ZCSe, and (e) CZCSe-1, (f) SAED pattern of CZCSe-1, (g) HRTEM image of CZCSe-1, (h–n) elemental colour mapping, and (o) spectra of CZCSe-1.

(Fig. 3(c–e)). The SAED pattern shown in Fig. 3(f) confirms the polycrystalline property of the material with the ring designated to the (111) and (311) plane of C/N–CeO_2 and the (111) plane of ZCSe, as verified from the XRD analysis.[21,25] Furthermore, the close interfacial interaction between C/N–CeO_2 and ZCSe is revealed by the HRTEM image shown in Fig. 3(g), with lattice fringes of 0.32 and 0.33 nm, which correspond to (311) and (111), respectively.[21] Also, the FESEM–EDX color mapping (Fig. 3(h–n)) and elemental spectra (Fig. 3(o)) confirm the presence of C, N, Ce, O, Cd, Zn, and Se elements in our fabricated material, in agreement with the XPS results.

3. Photocatalytic activity

3.1. Photocatalytic H_2O_2 production (PHPP)

The PHPP was investigated using ethanol as a sacrificial agent in an oxygen-saturated aqueous atmosphere under visible light illumination. Pristine C/N–CeO_2 and ZCSe show a comparatively lower PHPP of 1342.85 and 1590 μmol g^{-1} h^{-1}, respectively. Compared to CZCSe-0.5 (2667.12 μmol g^{-1} h^{-1}) and CZCSe-1.5 (2589.46 μmol g^{-1} h^{-1}) composites, the PHPP of the CZCSe-1 (2820.43 μmol g^{-1} h^{-1}) composite is much higher (Fig. 4(a)). As the ZCSe percentage increases, the PHPP first rises and subsequently drops. This is attributed to the high amount of ZCSe blocking the active sites, thus reducing the photocatalytic efficiency.[36,43] CZCSe-1 exhibits the highest PHPP (2820.43 μmol g^{-1} h^{-1}), 1.7 and 2.1-fold higher than those of C/N–CeO_2 and ZCSe, respectively, confirming the successful heterojunction formation between C/N–CeO_2 and ZCSe. The error bars indicate the good consistency of the PHPP of CZCSe-1.[5] Remarkably, CZCSe-1 outperforms the majority of the oxide-based semiconductor materials reported earlier in the literature, which is summarized in Table S6.† CZCSe-1 shows 0.11% solar-to-chemical energy conversion (SCC) efficiency and is presented in ESI section 4(b).† The PHPP is the combined outcome of the formation and decomposition of H_2O_2, which can be fitted using eqn (2).[5,8]

$$H_2O_2 \rightarrow \frac{k_f}{k_d}[1 - (-\exp -k_d t)] \quad (2)$$

Herein, the formation and decomposition rate constants are represented by the symbols k_f and k_d, respectively, corresponding to zero order and first order. Fig. 4(b) shows the fitted values of k_f and k_d values, among which CZCSe-1 exhibited the highest k_f and lowest k_d values, proving it as the best photocatalyst among all prepared samples. Further, the decomposition experiment of H_2O_2 was performed using a 100 μM concentration of H_2O_2, as it is inherently unstable under light illumination. Remarkably, 16% of H_2O_2 decomposition was recorded for CZCSe-1 after a two-hour light irradiation, highlighting the stability of H_2O_2 in this system (Fig. S8(b)†). For photocatalysts to be efficient for practical applications, cycling stability is as important as high production rates. The recycling stability of CZCSe-1 (Fig. S8(c)†) illustrates that the

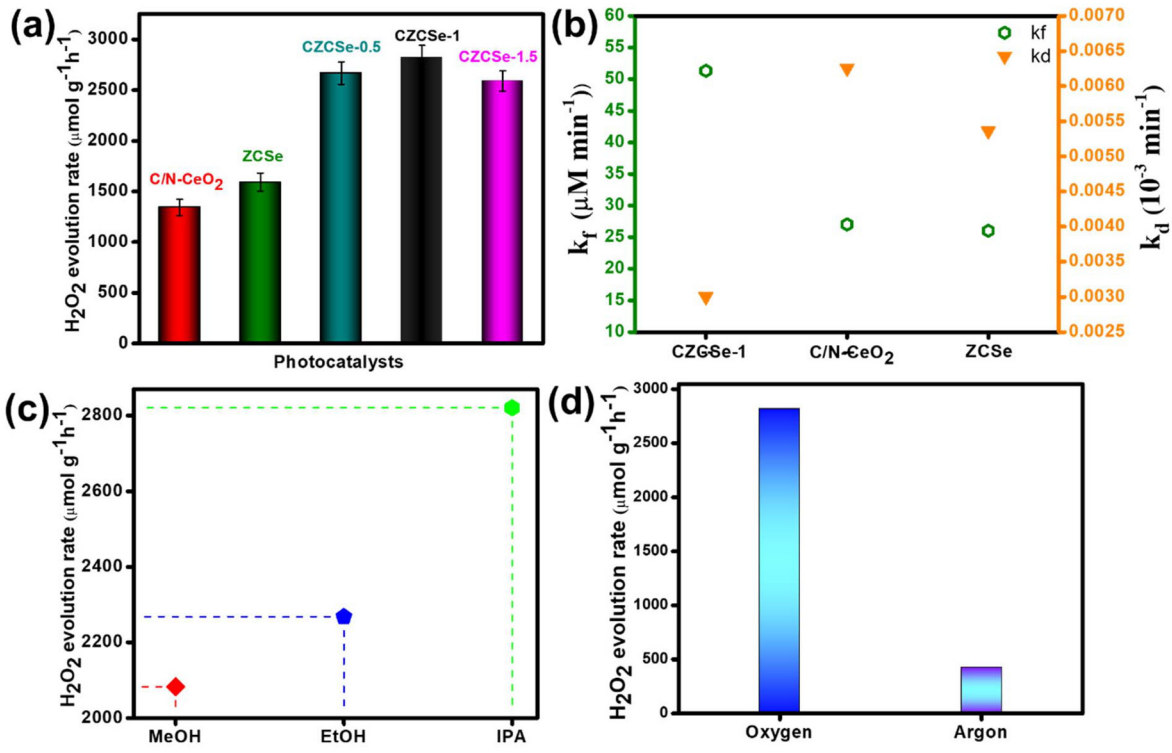

Fig. 4 (a) H_2O_2 production rate over different photocatalysts, (b) formation (k_f) and decomposition (k_d) rate constants of H_2O_2 production, (c) H_2O_2 production rate over different solvents, and (d) H_2O_2 production rate under different atmospheres.

PHPP of CZCSe-1 displays insignificant variation even after five cycles, suggesting the significant stability of CZCSe-1 for the PHPP. Afterward, PXRD (Fig. S12(a)†), FESEM (Fig. S12(b)†), FT-IR (Fig. S12(c)†), and UV (Fig. S12(d)†) analyses of CZCSe-1 were conducted to demonstrate the crystallinity, morphology, and chemical properties after the photocatalytic reaction, and the results were identical to those of CZCSe-1 before the experiment. Several controlled experiments were conducted to determine the reaction pathway for the PHPP. Moreover, the influence of an electron donor on H_2O_2 production is indispensable, and the outcomes are displayed in Fig. 4(c).† As illustrated, the maximum production rate was achieved for IPA, followed by EtOH and MeOH.[44] The high performance of IPA is due to the fact that being a secondary alcohol, it facilitates radical formation and stabilization, leading to higher yields of H_2O_2 compared to methanol and ethanol. In addition, its electron-donating capacity favors the ORR process in order to produce H_2O_2 efficiently.[8,45] As shown in Fig. 4(d), negligible H_2O_2 yield is recorded under dark conditions and in an Ar-saturated solution for CZCSe-1, revealing that H_2O_2 is produced from the photocatalytic O_2 reduction reaction.

To better understand the reaction pathways and identify the reactive oxygen species involved in the ORR, a series of quenching experiments were performed to examine the intermediate species implicated in the PHPP using CZCSe-1. DMSO, CA, pBQ, and TBA act as sacrificial agents for electrons, holes, superoxide, and hydroxyl radicals, respectively (Fig. S8(a)†).[3,24,46,47] The introduction of DMSO significantly diminished the PHPP of CZCSe-1, while the presence of CA generated more PHPP, indicating the role of electrons in the oxygen reduction reaction towards PHPP. Notably, the PHPP of CZCSe-1 abruptly diminished with the addition of pBQ; however, with the addition of TBA, the PHPP of CZCSe-1 moderately decreased. This implies that $O_2^{\bullet-}$ is a crucial intermediate reactive species in the PHPP of CZCSe-1, potentially allowing an indirect single e^- ORR pathway. Further, to obtain a better understanding of the reaction pathway, the PHPP of CZCSe-1 was analysed by employing other hole scavengers, such as methanol, ethanol, and IPA (Fig. 4(c)). The addition of the above hole scavengers improved the PHPP by potentially slowing down the decomposition of H_2O_2 and demonstrated that ORR by photogenerated electrons is the primary source of H_2O_2 generation.[6] Additionally, electron spin resonance (ESR) of CZCSe-1 was analysed in the presence of a spin-trapping reagent. 5,5-Dimethyl-1-pyroline *N*-oxide (DMPO) was used as a spin-trapping agent to trap the intermediate species such as $O_2^{\bullet-}$ and $OH^{\bullet}$ (Fig. S10(a and b)†). As illustrated in Fig. S10(b),† CZCSe-1 shows four characteristic peaks with 1 : 1 : 1 : 1 intensity, suggesting the formation of DMPO–$O_2^{\bullet-}$ under light illumination; however, the corresponding peak intensity is negligible in the dark.[8] The observation was further supported by the nitro blue tetrazolium (NBT) and terephthalic acid (TA) analysis, which were performed to confirm the formation of the respective intermediate radicals $O_2^{\bullet-}$ and $OH^{\bullet}$ (Fig. S9(a and b)†).[48,49] Therefore, it can be concluded from the ESR and NBT analysis that CZCSe-1 can efficiently facilitate an indirect single electron ORR pathway for PHPP, as illustrated in the following equations.

$$\text{C/N–CeO}_2\text{/ZCSe} \rightarrow e^-(\text{CB}) + h^+\ (\text{VB}) \quad \text{(I)}$$

$$O_2 + e^- \rightarrow O_2^{\bullet-} \quad \text{(II)}$$

$$O_2^{\bullet-} + e^- + 2H^+ \rightarrow H_2O_2 \quad \text{(III)}$$

Besides, the PHPP of CZCSe-1 could possibly be due to water oxidation by photogenerated holes and $OH^{\bullet}$ intermediate species. The dimerization of $OH^{\bullet}$ produces H_2O_2, which is stated as WOR. As C/N–CeO_2 possesses a VB potential (2.3 V) that is more positive than that of the electrode potential H_2O/$OH^{\bullet}$ (1.99 V *vs.* NHE), it can oxidize H_2O to $OH^{\bullet}$. The above results suggest two possible pathways for the PHPP that occur over CZCSe-1 (Scheme 2): (1) single-electron indirect ORR with $O_2^{\bullet-}$ as the intermediate; (2) direct oxidation of H_2O by photogenerated holes. Hereafter, both photogenerated electrons and holes efficiently participated in the reaction pathways, significantly decreasing the recombination rate of charge carriers. More significantly, in CZCSe-1, the S-Scheme heterojunction enhanced the photogenerated e^-–h^+ separation and migration, substantially promoting their photocatalytic activity.

$$\text{C/N–CeO}_2\text{/ZCSe} \rightarrow e^-(\text{CB}) + h^+\ (\text{VB}) \quad \text{(IV)}$$

$$OH^- + h^+ \rightarrow OH^{\bullet} \quad \text{(V)}$$

$$OH^{\bullet} + OH^{\bullet} \rightarrow H_2O_2 \quad \text{(VI)}$$

3.2. Photocatalytic O_2 evolution reaction (POER)

In addition to the above, POER is termed as a challenging and slow rate reaction, as it involves the $4e^-$–$4H^+$ coupling process.[9] All the synthesized materials were applied in the POE process under visible light irradiation, and the obtained result is displayed in Fig. 5(a). The maximum O_2 evolution rate (234.89 mmol g^{-1} h^{-1}) was shown by the best photocatalyst, CZCSe-1, with an ACE of 3.76%. The result could be attributed to the efficient charge separation and longer lifetime of the photocarriers, which are supported by the EIS, PL, and TRPL plots. Further, MOF-derived C/N–CeO_2 and CZCSe-1 composites hold specific interest due to the presence of defects (OVs), which are helpful in the formation of the intermediate O-atom during H_2O decomposition.[9] Moreover, the photostability of CZCSe-1 is demonstrated in Fig. 5(b), with a minute drop in the POE rate even after five consecutive cycles. A comparative table (Table S5†) of the POE rate of other metal oxides-based systems is provided for better correlation.

4. Mechanistic approach for photocatalytic H_2O_2 production

Based on the significant enhancement of the PHPP and PWO of CZCSe-1, a number of characterization techniques were employed to validate the proposed mechanism. Also, the photocatalytic performance is significantly influenced by the

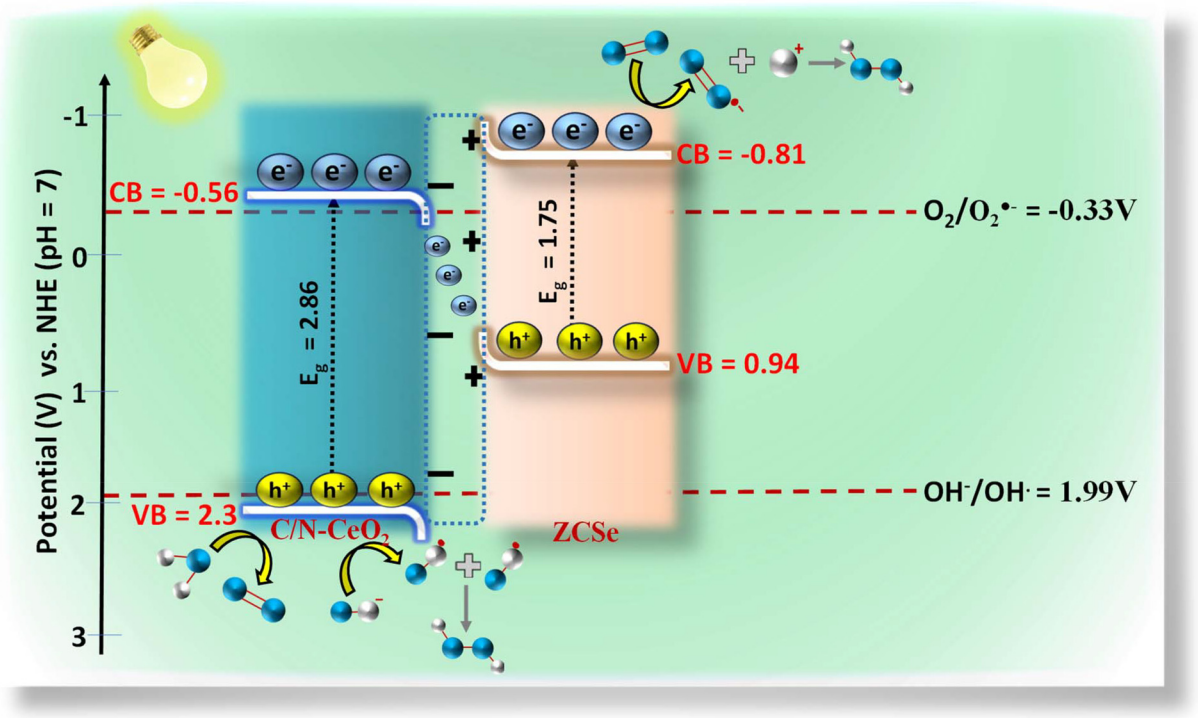

Scheme 2 Schematic of the S-scheme charge dynamics for H_2O_2 production and O_2 evolution.

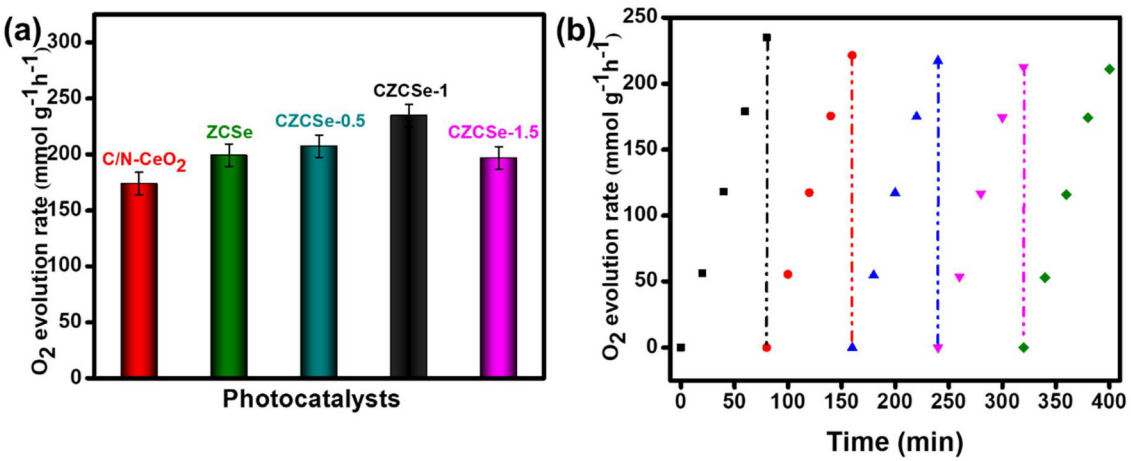

Fig. 5 (a) O_2 production rate over different photocatalysts and (b) recyclability test of CZCSe-1 for O_2 evolution.

optical properties and electronic structure of the composite materials. The UV-vis absorption spectroscopy of all synthesized materials was analysed and displayed in Fig. 6(a). As illustrated, the absorption tail of the parent C/N–CeO_2 extends from UV to the visible region because of the interband charge transfer (CT) between Ce^{3+}/Ce^{4+} and CT between O^{2-} (2p) E_{VB} to Ce^{4+} (4f) E_{CB}.[9,50] The neat ZCSe shows good absorption in the visible region with an absorption edge at around 750 nm.[5,21] Moreover, a significant phenomenon was observed for the composites in which their photoresponse and absorption gradually enhanced with an increase in the amount of ZCSe, and the optimum photoabsorption was found for CZCSe-1. The enhanced light-absorbing capability of the heterostructure with an ideal amount of ZCSe on C/N–CeO_2 revealed the firmly established heterostructure among the two neat components. Additionally, the Tauc plot was used to assess the band gap of neat materials (Fig. 6(b)) by plotting the energy and absorption values, which were found to be 2.86 and 1.75 eV for C/N–CeO_2 and ZCSe, respectively.[21,25] Further, a small-range scan of the valence band XPS (VB-XPS) plots can

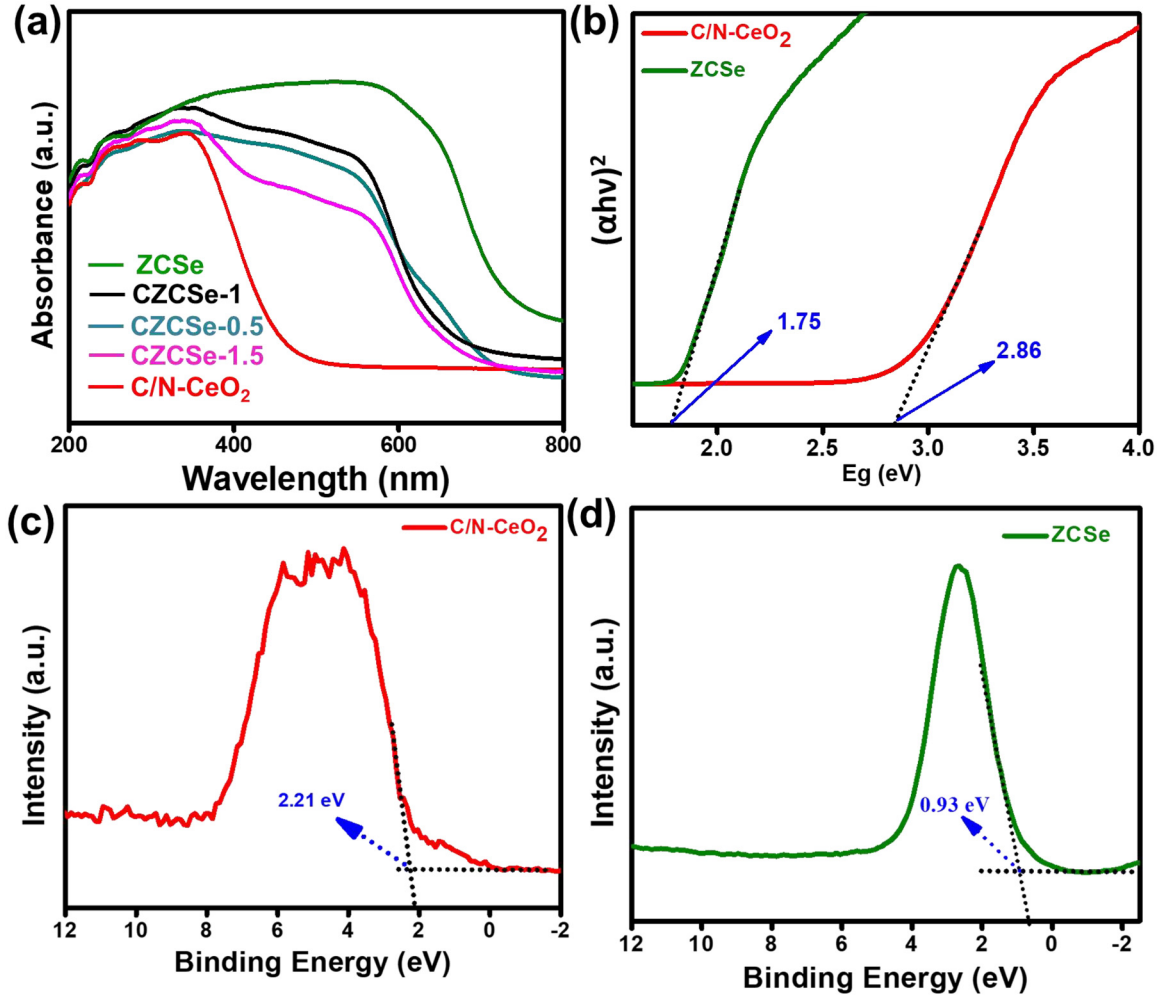

Fig. 6 (a) UV-Vis DRS spectra of all the synthesized photocatalysts, (b) Tauc plot of C/N–CeO_2 and ZCSe, and VB-XPS spectra of (c) C/N–CeO_2 and (d) ZCSe.

be used to determine the VB value of the semiconductors. The VB values of C/N–CeO_2 and ZCSe were determined to be 2.21 and 0.93 V, as depicted in Fig. 6(c) and (d), respectively. Thereafter, we perform the Mott–Schottky (MS) experiment to measure the band edge potentials of the photocatalysts, as these are also some essential parameters to describe the reaction mechanism. Fig. S11(a and b)† displays the flat band potential of C/N-CeO_2 and ZCSe as −0.65 V and −0.9 V *vs.* Ag/AgCl, respectively. The n-type character of the semiconductors was indicated by the positive slopes displayed by ZCSe and C/N–CeO_2.[28,51] The measured flat band potential with reference to the Ag/AgCl electrode at pH = 7 can be converted to the NHE scale by the following equation[16,24,50]

$$E_{(\mathrm{NHE})} = E_{\mathrm{Ag/AgCl}} + E^{\circ}_{\mathrm{Ag/AgCl}} - 0.0591\,(7\text{-pH}) \quad (3)$$

Here, $E^{\circ}_{\mathrm{Ag/AgCl}} = 0.197$ V at 25 °C and $E_{\mathrm{Ag/AgCl}}$ is the flat band potential of the standard hydrogen electrode. The fermi level (E_f) position of C/N–CeO_2 and ZCSe were calculated to be −0.46 and −0.71 V. Generally, the E_f value in the NHE scale of the n-type semiconductor was nearer to the CB position; hence, by considering a 0.1 V value variation, the CB potential of C/N–CeO_2 and ZCSe could be close to −0.56 V and −0.81 V (*vs.* NHE, pH = 7), respectively. Consequently, according to the expression,[52–54]

$$E_{\mathrm{CB}} = E_{\mathrm{VB}} - E_g \quad (4)$$

E_{CB} is the conduction band, E_{VB} is the valence band, and E_g denotes the bandgap energy. The E_{VB} values of C/N–CeO_2 and ZCSe were estimated to be about 2.3 and 0.94 V, respectively. Additionally, using the following formula, the VB potential of NHE may be determined based on the contact potential difference between the samples and the XPS analyzer[55]

$$E_{\mathrm{VB}}\text{-NHE} = \varphi + E_{\mathrm{VB}} - \mathrm{XPS} - 4.44 \quad (5)$$

E_{VB}-NHE is the VB potential in the NHE scale at pH = 7, φ is the work function of an electron with a value of 4.55 eV from the XPS analysis, and E_{VB}-XPS is the VB value calculated using the VB-XPS plots. Hence, the E_{VB}-NHE of C/N–CeO_2 and ZCSe is equal to 2.3 V and 0.94 V, respectively. C/N–CeO_2 and ZCSe were found to have bandgaps of 2.86 and 1.75 eV, respectively,

based on the results of the MS and XPS spectra investigations, which were found to be in good correlation with the bandgap values derived from the Tauc plot. To examine the interfacial charge transfer between the two materials, the work functions of C/N–CeO_2 and ZCSe were measured and calculated using the small-range scan of the VB-XPS plots. When the solid sample and metal sample holder of the XPS analyser were in good electrical contact with the balanced electron transfer, the Fermi levels of both the materials in the composite reached the same level. However, the kinetic energy of the e^- was altered due to the contact difference $\Delta V = \Phi - \varphi$ (φ is the work function obtained from the XPS analyser with the value equal to 4.55 eV, and Φ is the work function of the sample), thereby changing the binding energy of the electrons.[8,55] By measuring the change in the binding energy in a small range by XPS, ΔV could be gained from the spacing between the two inflection points (IPs) of the curves (Fig. S7(a and b)†), and then the Φ value of C/N–CeO_2 and ZCSe could be estimated as 6.38 and 5.28 eV, respectively. Therefore, on the basis of MS and VB-XPS values above, the energy band alignments of the heterojunction and the possible charge transfer pathway were proposed and illustrated in Scheme S1.† In contrast to ZCSe, a material with a smaller work function (5.55) and a higher Fermi level, C/N–CeO_2 had a bigger work function (6.38) and a lower Fermi level. Therefore, the electrons on ZCSe would naturally go to C/N–CeO_2 upon close contact until their Fermi levels reached equilibrium. At this point, an internal electric field (IEF) developed at the contact surface, where the opposite charges were accumulated on both sides.[56] The stimulation of IEF upon light irradiation increased the potential difference between C/N–CeO_2 and ZCSe by increasing the probability that the excited electrons on the CB of C/N–CeO_2 ($CB_{C/N-CeO_2}$) would transfer and recombine with the holes on the VB of ZCSe (VB_{ZCSe}).

Photoluminescence (PL) spectroscopy provides an effective way to determine the trapping, separation, and migration efficiency of excitons.[57–59] From the spectrum, the strong and intensified peak represents the fast recombination of e^-–h^+ pairs, whereas low and weaker PL intensity signifies delayed recombination of charge carriers.[60,61] The PL emission of all the synthesized samples was recorded by photoexcitation at 330 nm (Fig. 7(a)). Pure C/N–CeO_2 shows PL signals with peaks at around 429 and 540 nm, probably attributed to the OV and self-trapping excitations, respectively.[9,13] A reduction in the intensity can be noticed for composites (lowest for CZCSe-1), which indicates the lower recombination rate of the photogenerated charge carriers. Furthermore, the diminished PL intensity of pristine ZCSe signifies low photoexcitation

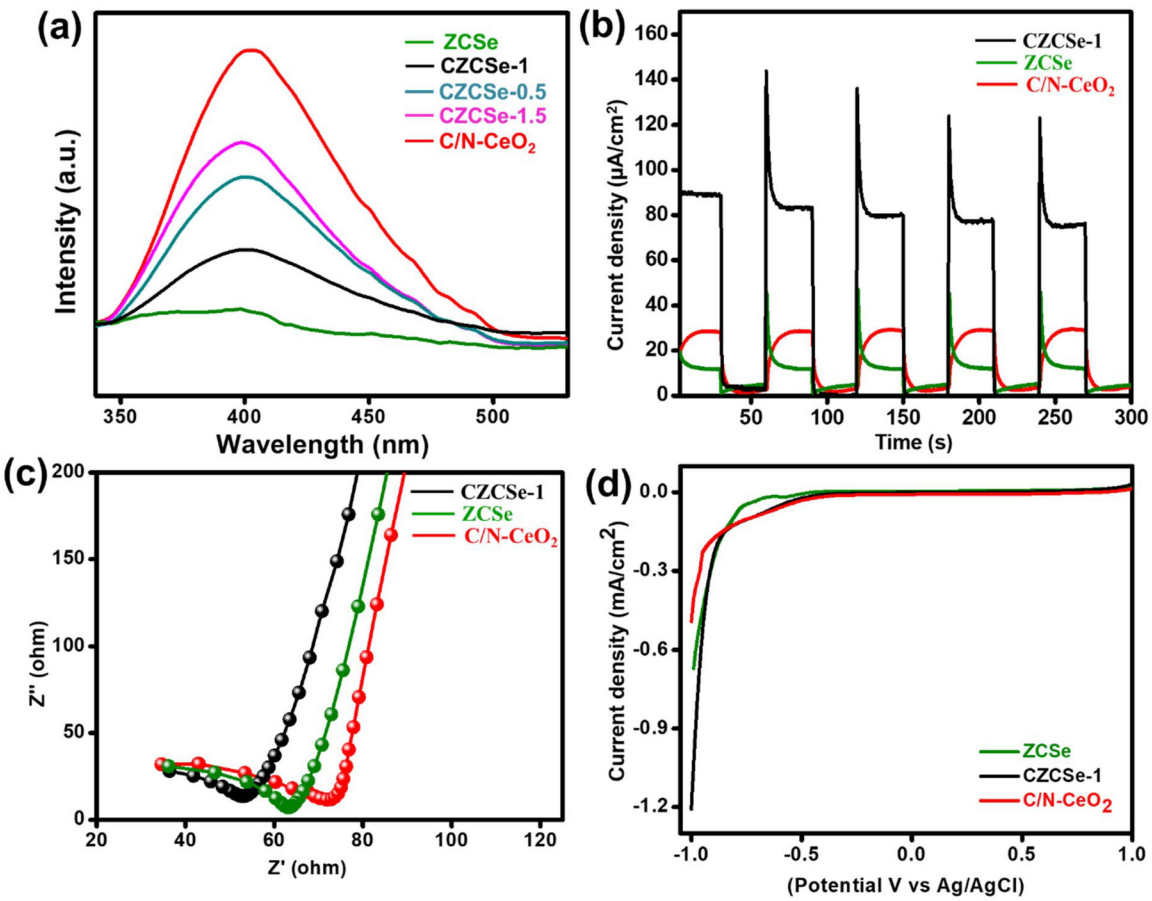

Fig. 7 (a) PL spectra of all synthesized photocatalysts, (b) transient photocurrent, (c) EIS, and (d) LSV curves of C/N–CeO_2, ZCSe and CZCSe-1.

efficiency in the particular region due to the quantum confinement effect.[8] Therefore, the outcomes suggest that in CZCSe-1, the photoexcited charge carriers are effectively separated and facilitate the execution of photocatalytic reactions at the respective ends of the semiconductors. Also, time-resolved photoluminescence (TRPL) analysis of C/N–CeO_2 and CZCSe-1 was carried out in order to extend the above discussion (Fig. S6†). The average lifetime of the photoexcited charge carriers was estimated by using the following equation,[25]

$$A + B_1 \exp(-t/\tau_1) \quad (6)$$

Here, all symbols correspond to their usual meaning.[42] As noted, the CZCSe-1 composite has the highest average lifetime (τ = 1.38 ns) as compared to that of neat C/N–CeO_2 (τ = 0.27 ns), providing evidence of the highest anti-recombination rate of excitons and photoactivity in the case of the CZCSe-1 composite. Further, we performed the transient photocurrent measurements to verify the separation, mobility, and lifetime of the photoinduced excitons. From the graph (Fig. 7(b)), the remarkably highest photocurrent density was recorded for the CZCSe-1 heterojunction compared to those of neat C/N–CeO_2 and ZCSe. Moreover, the analysis can be attributed to the enhanced segregation of photoinduced excitons, signifying that the excitons were generated effectively in CZCSe-1 and available for a longer time before they recombined. This improvement leads to the validation of a better charge carrier migration at the interface, establishing an n–n heterostructure between C/N–CeO_2 and ZCSe. Furthermore, the electrochemical impedance spectroscopy (EIS) technique for C/N–CeO_2, ZCSe, and CZCSe-1 composite materials under light irradiation is depicted in Fig. 7(c). Generally, from the arc radius of the Nyquist plot, we can assess the charge transfer resistance of the photocatalyst, and a lower resistance implies that the charge carriers can move more freely to participate in the photocatalytic reactions.[25,62,63] As shown in Fig. 7(c), the CZCSe-1 composite has the smallest semicircle arc, signifying the lowest charge transfer resistance and superior channelization of photoinduced excitons. The improved separation and migration of photogenerated charge carriers with boosted conductivity of the best composite material can be attributed to the formation of a 1D–0D S-scheme heterojunction.[64–68] As shown in Fig. 7(d), CZCSe-1 displayed the maximum cathodic current as compared to neat materials, suggesting the easy reduction of molecular oxygen to superoxide followed by H_2O_2 formation.[69,70]

Despite the clarity on the band structure and initial transfer of photogenerated charge carriers at the heterojunction interface, there is still a lack of other solid evidence regarding the formation of reactive intermediates involved during the photocatalytic process for the PWO and PHPP. In light of this, various quenchers, including p-BQ, TBA, CA, and DMSO, were employed to trap $O_2^{\bullet-}$, $^{\bullet}OH$, h^+, and e^-, respectively (Fig. S8(a)†). When DMSO and p-BQ were utilized as scavenging agents, as illustrated in Fig. S8(a),† a significant decrease in the PHPP efficiency was observed, which demonstrated the major role of e^- and $O_2^{\bullet-}$ for the production of H_2O_2 *via* the 1 e^- two-step process. However, employing TBA and CA as scavenging agents also impacted the PHPP rate, demonstrating the sufficient participation of $^{\bullet}OH$ and h^+ in the reaction. Moreover, the ESR spin trap technique was employed to ensure the involvement of $O_2^{\bullet-}$ and $^{\bullet}OH$ in the reaction process. Fig. S10(a) and S10(b)† demonstrate that in the dark, no $O_2^{\bullet-}$ or $^{\bullet}OH$ signals were detected. After exposure to visible light, radical signals emerged, signifying the formation of $O_2^{\bullet-}$ and $^{\bullet}OH$ radicals in the presence of CZCSe-1. Combined with the result of the trapping test and ESR analysis, we believe that H_2O_2 is produced in two ways, *i.e.*, (i) by the action of $O_2^{\bullet-}$ and H^+ at CB_{ZCSe} and (ii) by the recombination of two species of $^{\bullet}OH$ at $VB_{C/N-CeO_2}$. The calculated CB position of ZCSe (−0.81 V) and VB position of C/N–CeO_2 (2.3 V) is suitable for the production of $^{\bullet}O_2^-$ and $^{\bullet}OH$ radicals, as represented above.

Scheme 2 displays a plausible mechanism for an improved photocatalytic process based on the above data and discussion. The band structure analysis indicates that the CZCSe-1 nanohybrid exhibits a standard type-II heterojunction. Conversely, if that is the case, the holes on VB_{ZCSe} would not suitably have a higher oxidation potential (0.94 V) to generate $^{\bullet}OH$ ($OH^-/OH^{\bullet}$, 1.99 V), which is clearly in disagreement with the above experimental outcomes. The energy band structure, IEF, trapping test, and DMPO-ESR results were all combined to successfully clarify the most reasonable S-scheme charge transfer pathway. An internal electric field (IEF) was generated when C/N–CeO_2 and ZCSe were in contact, causing the downward and upward band bending movement of C/N–CeO_2 and ZCSe, respectively. Upon light illumination, electrons on $CB_{C/N-CeO_2}$ and holes on VB_{ZCSe} recombined with each other due to the combined interaction of IEF and band bending while keeping the holes and electrons with higher redox potentials on $VB_{C/N-CeO_2}$ and CB_{ZCSe}. The holes on $VB_{C/N-CeO_2}$ oxidised H_2O to O_2 and OH^- to $^{\bullet}OH$, while the electrons on CB_{ZCSe} reduced O_2 to $O_2^{\bullet-}$, which further reacts with H^+ to produce H_2O_2, as described in the above equations.

5. Conclusion

This study has demonstrated the successful fabrication of defect-induced C/N–CeO_2 nanorods with surface decorating ZCSe QDs using a simple reflux technique, which resulted in a significant enhancement of photocatalytic H_2O_2 production and O_2 evolution. When 1 mmol ZCSe (molar ratio of Zn/Cd is 1 : 1) was used, the CZCSe-1 sample exhibited the optimal H_2O_2 production (SCC = 0.11%) and O_2 evolution rate (ACE = 3.6%). The augmented photocatalytic activities may be attributed to the robust interaction between oppositely charged C/N–CeO_2 and ZCSe, not allowing the further decomposition of H_2O_2 into $^{\bullet}OH$. Also, the surface defects are responsible for the broad and intensified light absorption by CZCSe-1 and serve as the e^- trapping site, thus impeding the photocarrier recombination. The decreased EIS and PL signals, higher cathodic photocurrent, and maximum photoresponse phenomenon further explain the photocarrier generation, sep-

aration, and transport *via* the S-scheme charge dynamics verified through VB-XPS and EPR analyses. Hence, this investigation offers a simple fabrication technique of a 1D–0D heterojunction (C/N–CeO_2/ZCSe) with new perspectives of a novel S-scheme system towards photocatalytic H_2O_2 production and O_2 evolution.

Data availability

The data described in this article have been included as a part of the ESI.†

Conflicts of interest

The authors declare that they have no known competing financial interests or personal relationships that could have appeared to influence the work reported in this paper.

Acknowledgements

S 'O' A Deemed to be University, Bhubaneswar, Odisha's management and staff are thankfully acknowledged for their constant support and encouragement in this work.

References

1 B. Liu, C. Bie, Y. Zhang, L. Wang, Y. Li and J. Yu, *Langmuir*, 2021, **37**, 14114–14124.
2 R. S. Disselkamp, *Energy Fuels*, 2008, **22**, 2771–2774.
3 B. P. Mishra, L. Biswal, S. Das, L. Acharya and K. Parida, *Langmuir*, 2023, **39**, 957–971.
4 Y. Xiao, Y. Tao, Y. Jiang, J. Wang, W. Zhang, Y. Liu, J. Zhang, X. Wu and Z. Liu, *Sep. Purif. Technol.*, 2023, **304**, 122385.
5 J. Sahu, S. Mansingh, B. P. Mishra, D. Prusty and K. Parida, *Dalton Trans.*, 2023, **52**, 16525–16537.
6 A. Ray, S. Subudhi, S. P. Tripathy, L. Acharya and K. Parida, *Adv. Mater. Interfaces*, 2022, **9**, 2201440.
7 L. Acharya, G. Swain, B. P. Mishra, R. Acharya and K. Parida, *ACS Appl. Energy Mater.*, 2022, **5**, 2838–2852.
8 K. K. Das, U. A. Mohanty, R. Mohanty, P. P. Sarangi, D. P. Sahoo and K. Parida, *ACS Appl. Energy Mater.*, 2024, **7**, 6360–6375.
9 S. Mansingh, S. Subudhi, S. Sultana, G. Swain and K. Parida, *ACS Appl. Nano Mater.*, 2021, **4**, 9635–9652.
10 S. Zhang, J. Guo, W. Zhang, H. Gao, J. Huang, G. Chen and X. Xu, *ACS Sustainable Chem. Eng.*, 2021, **9**, 11479–11492.
11 Y. Pu, Y. Luo, X. Wei, J. Sun, L. Li, W. Zou and L. Dong, *Appl. Catal., B*, 2019, **254**, 580–586.
12 X. Tao, W. Cong, L. Huang and D. Xu, *J. Alloys Compd.*, 2019, **805**, 1060–1070.
13 S. Sultana, S. Mansingh and K. M. Parida, *J. Phys. Chem. C*, 2018, **122**, 808–819.
14 C. Zhu, Y. Wang, Z. Jiang, F. Xu, Q. Xian, C. Sun, Q. Tong, W. Zou, X. Duan and S. Wang, *Appl. Catal., B*, 2019, **259**, 118072.
15 R. Bibi, H. Huang, M. Kalulu, Q. Shen, L. Wei, O. Oderinde, N. Li and J. Zhou, *ACS Sustainable Chem. Eng.*, 2019, **7**, 4868–4877.
16 G. S. More and R. Srivastava, *Ind. Eng. Chem. Res.*, 2021, **60**, 12492–12504.
17 G. S. More and R. Srivastava, *Ind. Eng. Chem. Res.*, 2021, **60**, 12492–12504.
18 C. Zhao, X. Li, L. Yue, S. Yuan, X. Ren, Z. Zeng, X. Hu, Y. Wu and Y. He, *J. Alloys Compd.*, 2023, **968**, 171956.
19 D. A. Hines and P. V. Kamat, *Am. Chem. Soc.*, 2014, **6**, 3041–3057.
20 M. Yang, Y. Wang, Y. Ren, E. Liu, J. Fan and X. Hu, *J. Alloys Compd.*, 2018, **752**, 260–266.
21 J. Qin, B. Liu, K. H. Lam, S. Song, X. Li and X. Hu, *ACS Sustainable Chem. Eng.*, 2020, **8**, 17791–17799.
22 N. X. Ca, H. T. Van, P. V. Do, L. D. Thanh, P. M. Tan, N. X. Truong, V. T. K. Oanh, N. T. Binh and N. T. Hien, *RSC Adv.*, 2020, **10**, 25618–25628.
23 B. Ng, L. K. Putri, X. Y. Kong, Y. W. Teh and P. Pasbakhsh, *Adv. Sci. (Weinh)*, 2020, **7**, 1903171.
24 L. Acharya, S. Nayak, S. P. Pattnaik, R. Acharya and K. Parida, *J. Colloid Interface Sci.*, 2020, **566**, 211–223.
25 B. P. Mishra, L. Acharya, S. Subudhi and K. Parida, *Int. J. Hydrogen Energy*, 2022, **47**, 32107–32120.
26 J. Panda, P. Behera, S. Subudhi, S. P. Tripathy, G. Swain, S. Dash and K. Parida, *Mater. Adv.*, 2024, **5**, 4865–4877.
27 Y. Kageshima, Y. Gomyo, H. Matsuoka, H. Inuzuka, H. Suzuki, R. Abe, K. Teshima, K. Domen and H. Nishikiori, *ACS Catal.*, 2021, **11**, 8004–8014.
28 L. Wei, D. Zeng, X. He, L. Wang, Y. Bao, G. He, T. Fujita, W.-J. Ong, L. Wei, D. Zeng, X. He, L. Wang, Y. Bao, G. He, T. Fujita and W.-J. Ong, *Adv. Energy Sustainability Res.*, 2022, **3**, 2100210.
29 G. Swain, S. Sultana and K. Parida, *ACS Sustainable Chem. Eng.*, 2020, **12**, 4848–4862.
30 S. D. Senol, O. Ozturk and C. Terzioğlu, *Ceram. Int.*, 2015, **41**, 11194–11201.
31 Y. Zhang, J. Shi, Z. Huang, X. Guan, S. Zong, C. Cheng, B. Zheng and L. Guo, *Chem. Eng. J.*, 2020, **401**, 126135.
32 P. Babu, S. Mohanty, B. Naik and K. Parida, *ACS Appl. Energy Mater.*, 2018, **1**, 5936–5947.
33 B. Thi Thu Hien, *J. Mater. Sci.*, 2028, **6**, 218–222.
34 M. Verma, A. Kaswan, D. Patidar, K. B. Sharma and N. S. Saxena, *J. Mater. Sci.: Mater. Electron.*, 2016, **27**, 8871–8878.
35 S. Subudhi, G. Swain, S. P. Tripathy and K. Parida, *Inorg. Chem.*, 2020, **59**, 9824–9837.
36 G. Murugadoss, D. D. Kumar, M. R. Kumar, N. Venkatesh and P. Sakthivel, *Sci. Rep.*, 2021, **11**, 8398.
37 S. Subudhi, G. Swain, S. P. Tripathy and K. Parida, *Inorg. Chem.*, 2020, **59**, 9824–9837.
38 W. Zou, B. Deng, X. Hu, Y. Zhou, Y. Pu, S. Yu, K. Ma, J. Sun, H. Wan and L. Dong, *Appl. Catal., B*, 2018, **238**, 111–118.

39 R. M. Rakhmatullin, V. V. Semashko, S. L. Korableva, A. G. Kiiamov, A. A. Rodionov, R. Tschaggelar, J. A. Van Bokhoven and C. Paun, *Mater. Chem. Phys.*, 2018, **219**, 251–257.
40 S. Maiti, T. Dhawa, A. K. Mallik and S. Mahanty, *Sustainable Energy Fuels*, 2017, **1**, 288–298.
41 G. Pacchioni, *ChemPhysChem*, 2003, **4**, 1041–1047.
42 D. P. Sahoo, S. Patnaik and K. Parida, *ACS Omega*, 2019, **4**, 14721–14741.
43 P. Behera, A. Ray, S. P. Tripathy, L. Acharya, S. Subudhi and K. Parida, *J. Photochem. Photobiol., A*, 2023, **436**, 114415.
44 A. Ray, S. Sultana, S. P. Tripathy and K. Parida, *ACS Sustainable Chem. Eng.*, 2021, **9**, 6305–6317.
45 J. Zhang, L. Zheng, F. Wang, C. Chen, H. Wu, S. A. K. Leghari and M. Long, *Appl. Catal., B*, 2020, **269**, 118770.
46 X. Geng, L. Wang, L. Zhang, H. Wang, Y. Peng and Z. Bian, *Chem. Eng. J.*, 2021, **420**, 129722.
47 Y. Li, S. Wan, W. Liang, B. Cheng, W. Wang, Y. Xiang, J. Yu and S. Cao, *Small*, 2024, **20**, 2312104.
48 N. Kaur, J. Singh, S. Kumar, P. Singh, S. Al-Rashed, H. Kaur and M. Rawat, *J. Mater. Sci.: Mater. Electron.*, 2020, **31**, 21233–21247.
49 A. Behera, D. Kandi, S. Sahoo and K. Parida, *J. Phys. Chem. C*, 2019, **123**, 17112–17126.
50 P. Mishra, A. Behera, D. Kandi, S. Ratha and K. Parida, *Inorg. Chem.*, 2020, **59**, 4255–4272.
51 C. Jiang, H. Wang, Y. Wang and H. Ji, *Appl. Catal., B*, 2020, **277**, 119235.
52 S. P. Tripathy, S. Subudhi, A. Ray, P. Behera, G. Swain, M. Chakraborty and K. Parida, *Langmuir*, 2023, **39**, 7294–7306.
53 B. P. Mishra and K. Parida, *J. Mater. Chem. A*, 2021, **9**, 10039–10080.
54 G. Swain, S. Sultana and K. Parida, *Inorg. Chem.*, 2019, **58**, 9941–9955.
55 L. Biswal, S. Nayak and K. Parida, *Catal. Sci. Technol.*, 2021, **11**, 1222–1248.
56 R. Sun, Z. Zhu, N. Tian, Y. Zhang and H. Huang, *Angew. Chem., Int. Ed.*, 2024, **63**, e202408862.
57 X. Li, J. Xiong, X. Gao, J. Ma, Z. Chen, B. Kang, J. Liu, H. Li, Z. Feng and J. Huang, *J. Hazard. Mater.*, 2020, **387**, 121690.
58 S. Subudhi, S. P. Tripathy and K. Parida, *Catal. Sci. Technol.*, 2021, **11**, 392–415.
59 S. Subudhi, S. P. Tripathy and K. Parida, *Inorg. Chem. Front.*, 2021, **8**, 1619–1636.
60 S. P. Tripathy, S. Subudhi and K. Parida, *Coord. Chem. Rev.*, 2021, **434**, 213786.
61 D. P. Sahoo, S. Patnaik and K. Parida, *ACS Omega*, 2019, **4**, 14721–14741.
62 P. Babu, S. Mohanty, B. Naik and K. Parida, *ACS Appl. Energy Mater.*, 2018, **1**, 5936–5947.
63 S. P. Tripathy, S. Subudhi, A. Ray, P. Behera, A. Bhaumik and K. Parida, *Langmuir*, 2022, **38**, 1766–1780.
64 S. P. Tripathy, S. Subudhi, A. Ray, P. Behera, J. Panda, S. Dash and K. Parida, *J. Colloid Interface Sci.*, 2023, **629**, 705–718.
65 S. Wang, B. Zhu, M. Liu, L. Zhang, J. Yu and M. Zhou, *Appl. Catal., B*, 2019, **243**, 19–26.
66 H. Zhang and X. Bai, *Appl. Catal., B*, 2021, **298**, 120516.
67 M. Karimia, S. Sadeghia, R. G. Gavinehroudi, H. Mohebali, A. Mahjoub and A. Heydari, *New J. Chem.*, 2021, **45**, 6671–6681.
68 S. Yuan, X. Liang, Y. Zheng, Y. Chu, X. Ren, Z. Zeng, G. Nan, Y. Wu and Y. He, *J. Colloid Interface Sci.*, 2024, **670**, 373–384.
69 M. Karimia, S. Sadeghia, R. G. Gavinehroudi, H. Mohebali, A. Mahjoub and A. Heydari, *New J. Chem.*, 2021, **45**, 6671–6681.
70 T. Jiang, K. Wang, T. Guo, X. Wu and G. Zhang, *Chin. J. Catal.*, 2020, **41**, 161–169.